Ultra-high specific surface area spherical FePO$_x$/SiO$_2$ aerogel with excellent mechanical properties for the highly selective direct oxidation of CH$_4$ to HCHO

Kunmeng Zhu[a,b], Fuwei Gao[c], Zhiyang Zhao[a], Jian Ren[a], Javier Lasobras[b], Xiaodong Shen[a]*, Sheng Cui[a]*, Miguel Menéndez[b]*

a State Key Laboratory of Materials-Oriented Chemical Engineering, College of Materials Science and Engineering, Nanjing Tech University, Nanjing, China

b Catalysis, Molecular Separations and Reactor Engineering Group (CREG), Aragon Institute of Engineering Research (I3A), University of Zaragoza, Zaragoza, Spain

c Shengli Oilfield Huaan Thermal Engineering Company with Limited Liability, Dongying, China

*Corresponding Authors

Tel.: +86 25 83587234; fax: +86 25 83221690

E-mail address: xdshen@njtech.edu.cn (X. Shen)

Tel.: +86 25 83587234; fax: +86 25 83221690

E–mail address: scui@njtech.edu.cn (S. Cui)

Tel.: +34 976 761152; fax: +34 976 762043

E-mail address: qtmiguel@unizar.es (M. Menéndez)

Abstract

Silica aerogels, characterized by their high porosity and substantial specific surface area, are suitable for applications as catalysts or catalyst supports. The simultaneous attainment of a substantial specific surface area and robust mechanical properties in aerogel materials remains a formidable challenge in material synthesis. Spherical FePO$_x$/SiO$_2$ aerogel materials were synthesized employing a combination of heating reflux, the sol-gel technique, and supercritical ethanol drying. These composites

demonstrate an exceptional specific surface area, uniformly dispersed active components, shape controllability, and superior mechanical strength. A noteworthy enhancement in both specific surface area (1175 m^2/g) and compressive modulus (7.56 MPa) surpasses many findings reported in extant literature. Under conditions of a reaction temperature at 650°C and a flow rate of 97.5 mL/min, the HCHO selectivity and yield for 4 wt.% $FePO_x$/SiO_2 aerogel were 18.3 and 4.2 times, respectively, higher than those of 4 wt.% $FePO_x$/SiO_2 particles. These composites manifest significant selectivity towards the direct catalytic oxidation of CH_4 to HCHO.

Keywords:

SiO_2 aerogel; Sol-gel method; High specific surface area; Mechanical strength; Methane oxidation

1. Introduction

Silica aerogels are recognized as the materials with the lowest density among known solids, typically produced via supercritical drying[1-4] or freeze drying[5-7]. During the drying phase, liquids are gradually supplanted by gases, ensuring the preservation of an integral skeletal structure with minimal collapse. Such a unique porous skeletal design bestows upon the aerogel attributes like remarkably low density, elevated porosity, reduced thermal conductivity, and high specific surface area[8-11]. These properties earmark aerogels for promising applications in areas like thermal insulation[12-14], optics[15, 16], sensing[17-19], catalysis[20, 21], and supercapacitors[22, 23], among others[24, 25]. Particularly in catalysis, aerogels can significantly influence liquid-solid and gas-solid catalytic reactions as catalysts or as catalyst supports.[26-28]. Synthesized through the sol-gel technique, aerogels can be modulated by adjusting components and proportions, controlling their composition, content, structure, and degree of dispersion, thereby tailoring them for specific reactions[29-34]. Nonetheless, the interlinking of nanoparticles that creates the skeletal structure and high porosity also introduces challenges such as the aerogel's inherent brittleness and tendency to crumble[35, 36]. The introduction of composite components

in aerogels typically results in reduced porosity and specific surface area, consequently constraining the versatility of aerogel applications.

Recent research has highlighted advancements in enhancing the specific surface area and mechanical attributes of aerogel composites. Yu et al.[37] integrated mesoporous Al_2O_3-SiO_2 aerogel into the macropores of quartz fiber via sol-gel impregnation. The resulting quartz fiber/Al_2O_3-SiO_2 aerogel composite exhibited a specific surface area of 580.5 m^2/g and a compressive strength of 0.85 MPa. Similarly, Lei et al.[38] fabricated SiO_2/GO composite aerogel monoliths using sol-gel technology. The interfacial synergy between GO nanosheets and the SiO_2 matrix enhanced the composite's compressive modulus by 0.156 MPa, albeit with a reduction in specific surface area by 277 m^2/g. Using triacrylate cross-linking to cross-link the silica surface, Maleki et al. managed to enhance mechanical properties, resulting in an optimized APD aerogel with a specific surface area of 53.1 m^2/g and an approximate twofold increase in mechanical strength[39]. Through process optimization and the introduction of reinforcing components or cross-linking modifications, researchers have augmented both the structure and mechanical attributes of aerogels[40-42]. However, the concurrent attainment of high porosity, specific surface area, and optimal mechanical properties remains challenging. Additionally, the bulk-form aerogel produced via conventional methods is not ideally suited for regular reactor applications[43, 44].

In this study, a novel aerogel preparation technique was introduced. Using the sol-gel method followed by ethanol supercritical drying, spherical $FePO_x$/SiO_2 aerogel (FPSA) catalyst materials characterized by an ultra-high specific surface area and superior mechanical properties were fabricated. The $FePO_x$ active component renowned for its marked advantage in catalytic methane processes[45, 46]. Characterization shows that $FePO_x$ is dispersed uniformly within the SiO_2 aerogel support possessing a vast specific surface area. This uniform distribution contributes to the catalytic activity of the composite material. The resultant FPSA boasts a high surface area, optimal dispersion of active components, a controllable morphology, and a robust, intact structure. Notably, its specific surface area and mechanical properties surpass most documented research findings. This composite catalyst material not only augments the specific surface area

and mechanical properties but also exhibits heightened HCHO selectivity during the direct catalytic oxidation of methane to HCHO.

2. Experimental section

2.1. Synthesis

2.1.1. Preparation of sol

Deionized water, ethanol, and nitric acid were mixed uniformly in a volume ratio of 60:40:1 to obtain an acidic solution. Tetraethyl orthosilicate (TEOS) was dissolved in 12 mL of ethanol and stirred evenly at room temperature. Slowly added 8 mL of acidic solution dropwise, continued to stir for 10 min, and then stirred and heated to reflux at 50 °C for 30 min, yielding solution A. 6 mL of deionized water was mixed with 18 mL of ethanol, 7 g of urea was dissolved in it, and stirred for 30 min at room temperature, which was recorded as solution B. Fe $(NO_3)_3 \cdot 9H_2O$ and $NH_4H_2PO_4$ with a molar ratio of Fe: P=1:1 were dissolved in 8 mL of deionized water, stirred evenly at room temperature, and recorded as solution C. Solution A was slowly added to the stirring solution C, mixed and stirred at room temperature for 30 min. Slowly added solution B, stirred at room temperature for 10 min, then transferred to a heating and refluxing device, stir and reflux at 80°C. The solution is in the form of a viscous sol to obtain a composite sol.

2.1.2. Sol forming spherical gel

The polydimethylsiloxane (PDMS) was elevated to 80°C. Upon temperature stabilization, the composite sol was meticulously dispensed into PDMS via a dropper. Over time, the sol droplets underwent gelation within PDMS, forming spherical entities. These spheres were extracted, and several rounds of deionized water rinses were performed to remove residual PDMS. These cleaned spheres were then transferred to ethanol solution, subjected to aging at 50°C, with ethanol solution being replaced thrice daily over a span of 4 days to facilitate solvent exchange. Following this, the spheres were taken out and supercritical dried with ethanol to obtain spherical aerogels. Post calcination at 650°C for 6 h, FPSA was obtained. Samples 4 wt.% $FePO_x/SiO_2$ aerogel,

8 wt.% FePO$_x$/SiO$_2$ aerogel and 16wt. % FePO$_x$/SiO$_2$ aerogel with different FePO$_x$ loadings were denoted as 4FPSA, 8FPSA and 16FPSA. For comparison, the same preparation process was used to synthesize pure SiO$_2$ aerogel (SA), and precipitated SiO$_2$ was used as a support to prepare 4 wt.% FePO$_x$/SiO$_2$ particles (4FPSP) by impregnation method.

2.2. Characterizations

Scanning electron microscopy (SEM) was performed by ZEISS GeminiSEM 300 to analyze the morphology of the materials. Transmission electron microscopy (TEM) images and high-resolution transmission electron microscopy (HRTEM) were performed on a JEOL JEM 2100F. Using an X-ray powder diffractometer (Rigaku Ultimate IV) with Cu-Kα radiation (λ= 1.5418 Å), powder X-ray diffraction (XRD) was measured in the 2θ range of 10° to 80° to analyze the phase and crystal structure of the material. Fourier Transform Infrared (FTIR) was tested using a Thermo Scientific Nicolet iS20 in the range of 400~2000 cm^{-1} to analyze the chemical composition of the samples. The specific surface area and pore size distribution of catalyst were measured by V-Sorb 2800P specific surface area and pore size analyzer, and analyzed by the Brunauer-Emmet-Teller (BET) test method. Mechanical performance was determined on a universal testing machine (DECCA-1, GB/T13480) stand at a constant compression rate of 0.2 mm/min. X-ray photoelectron spectroscopy (XPS) analysis was performed on the XPS Spectrometer Kratos AXIS Supra to study the elemental and valence composition of the material. The H$_2$ temperature programmed reduction (H$_2$-TPR) test was performed using a Micromeritics AutoChem II 2920 instrument and a TCD detector. Before starting the test, 0.1 g of the sample was put into the instrument and pure H$_2$ was passed through it. The temperature was raised to 200°C to pretreat the sample for 1 h, and the test was started after cooling down to 100°C. 10% H$_2$ in H$_2$-Ar mixed gas was introduced and heated to 800°C at a heating rate of 10 °C/min.

2.3. Catalytic activity

The catalytic reaction experiment was completed in a self-made fixed bed reactor

(quartz tube with a diameter of 1 cm). The working temperature was monitored and controlled by contacting the fixed bed with a thermocouple and connecting it with an electric furnace. The schematic diagram of the test system is shown in Fig. 1 In a typical catalytic reaction, the catalyst mass was 0.6 g. Before the catalytic reaction started, the evaporator was turned on to preheat, and the DINKO water injection pump was turned on after the temperature was stable. The deionized water was converted into water vapor in the evaporator and discharged. At the same time, the fixed-bed reactor containing the catalyst was heated up to the working temperature at a heating rate of 10 °C/min under a protective atmosphere of N_2. The flow rates of N_2, O_2 and CH_4 was controlled using the Brooks 5850 TR flow controller. After the temperature of the reactor and the discharge of water vapor were stabilized, the valve was turned to let the mixed gas pass into the catalytic bed, and the catalytic reaction test was started. The non-condensing reaction products were analyzed in a gas chromatograph (GC-CP3800 Varian with TCD detector). The condensed products were collected by an ice-bath condensation unit and analyzed in a gas chromatograph (GCMS-QP 2010 Shimadzu) connected to a mass spectrometer.
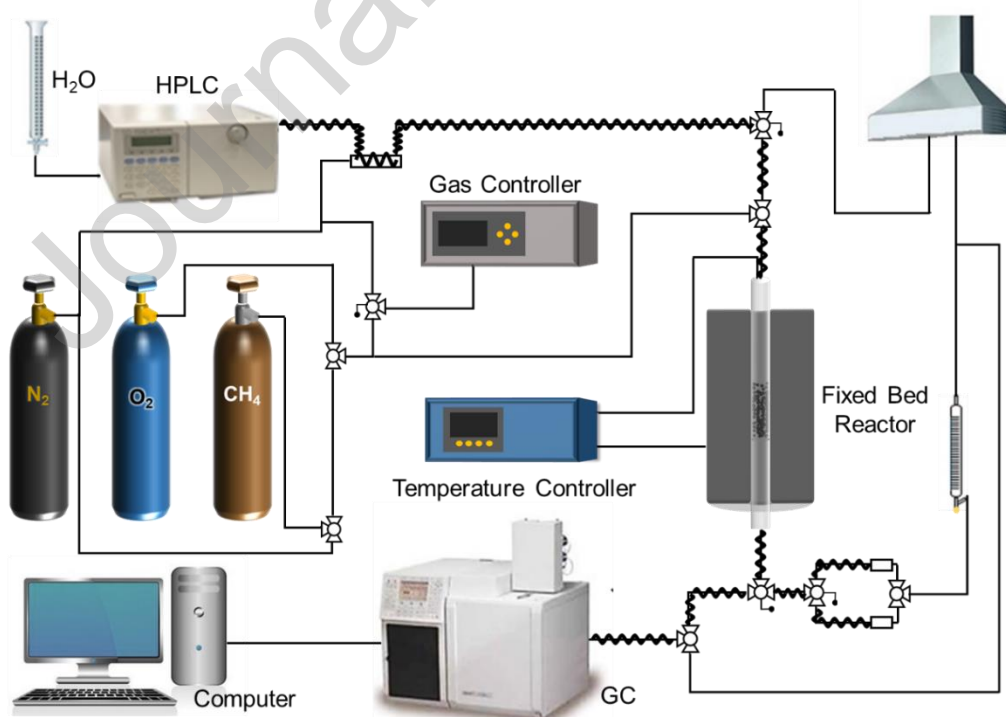

Fig. 1. The schematic diagram of the test system.

The results related to conversion and selectivity were calculated based on the results of

online monitoring of gas products and the identification and quantification of products in the condenser. The calculation of yield was obtained by multiplying the CH_4 conversion and the average selectivity of HCHO.

The calculation formula for the conversion of CH_4.

$$\chi_{CH_4} = \frac{nCH_2O + nCO_2 + nHCHO + 2nEtOH + nCO + nHCHO(liq) + 2nEtOH(liq) + nCH_2O(liq)}{nCH_4 \text{ totals}}$$

$$n_{CH_4} \text{ totals} = \frac{nCH_4}{min} \cdot \text{experiment time}$$

The calculation formula for HCHO selectivity.

$$S_{CH_4 \to HCHO} = \frac{nHCHO + nHCHO(liq)}{nCO_2 + nCO + nCH_2O + 2nEtOH + nCH_2O(liq) + 2nEtOH(liq)}$$

The calculation formula for HCHO yield.

$$Y_{CH_4 \to HCHO} = S_{CH_4 \to HCHO} \cdot \chi_{CH_4}$$

3. Results and discussion

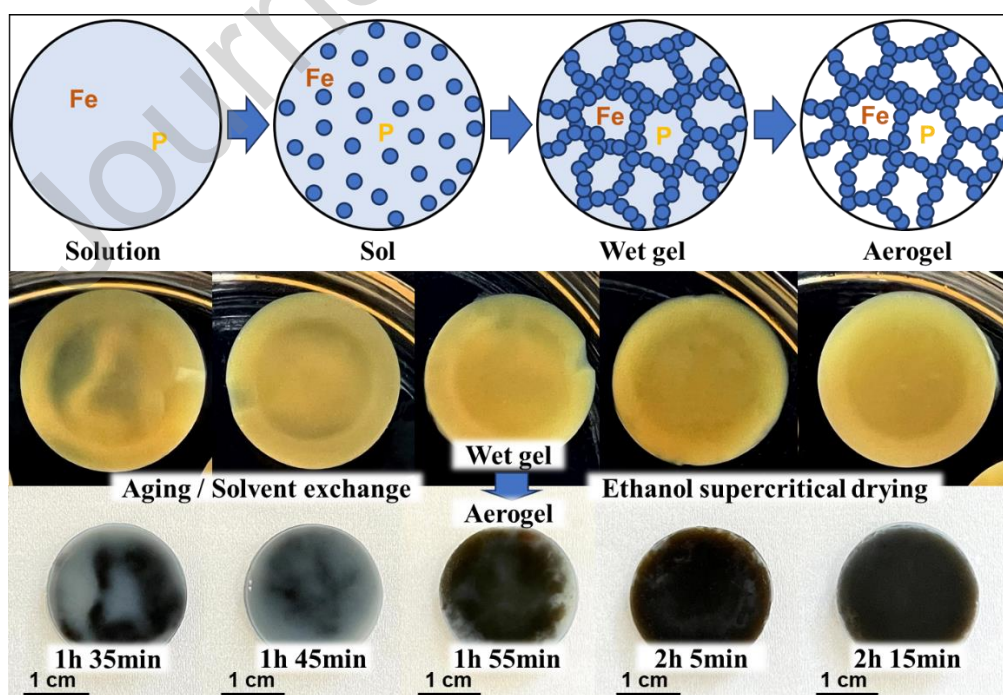### 3.1. Material Photographs

Fig. 2. Gel formation mechanism and aerogel samples with different reflux times.

The synthesis of composites involves the gelation of mixed sols, leading to the formation of wet gels. This is followed by aging and drying to produce aerogels. During preparation, the duration of the heating reflux critically influences the sol-to-gel transition time and the resultant material structure. It is imperative to circumvent issues such as premature sol solidification due to inadequate reflux durations and undesired gelation arising from prolonged reflux. Fig. 2 illustrates the gel formation mechanism and the block samples post different reflux durations. A noticeable improvement in sample uniformity correlates with extended reflux times. The sol initiated solidification when the heating reflux duration surpassed 2 h 15 min, warranting the removal of the sol at 2 h 10 min to facilitate subsequent droplet experiments. Fig. 3 delineates the preparation process of spherical 4FPSA. The sol droplets assume a spherical shape due to surface tension dynamics when the sol drops into PDMS. Given the elevated temperature of PDMS, these spheroidal sols commence gelation while descending, culminating in their settling at the bottom of the PDMS. At this juncture, the material's internal structure remains incompletely cross-linked. The subsequent transfer of the gel and multiple solvent replacements over a defined duration also contribute to material aging. Consequently, the internal structure achieves enhanced maturity and integrity. The final spherical aerogel results from supercritical ethanol drying followed by calcination. The spherical aerogel has a size of about 3 mm and can be modulated based on the volume of sol dispensed in a single instance.
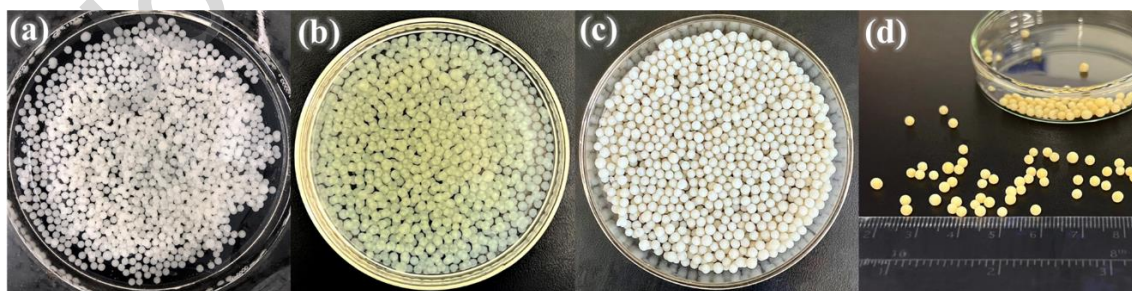

Fig. 3. Preparation process of spherical 4FPSA (a) gel in PDMS, (b) gel after solvent replacement, (c) spherical aerogel, (d) calcined spherical aerogel.

3.2. Morphological analysis

Fig. 4 displays the SEM image and elemental distribution of 4FPSA as observed

through EDS mapping. Fig. 4(a~d) reveal that 4FPSA exhibits a honeycomb-like morphology with a profusion of pores. Silica nanoparticles interconnect to form a characteristic "pearl-like" framework, leading to continuous pores primarily of mesoporous nature. Pore sizes predominantly fall within the 10-30 nm range. Fig. 4 (i~j) illustrate a uniform distribution of Si and O signals within the material, with silicon oxide serving as a supportive matrix ensuring an evenly dispersed platform for the active components. Although Fig.4(g) and 4(h) show that the counts for Fe and P signals are comparatively low, as depicted in Fig. 4(f), they are evenly distributed within the silicon oxide support. For a catalyst material, such high dispersion of the active component on its surface augments both its catalytic efficiency and the selectivity for HCHO.
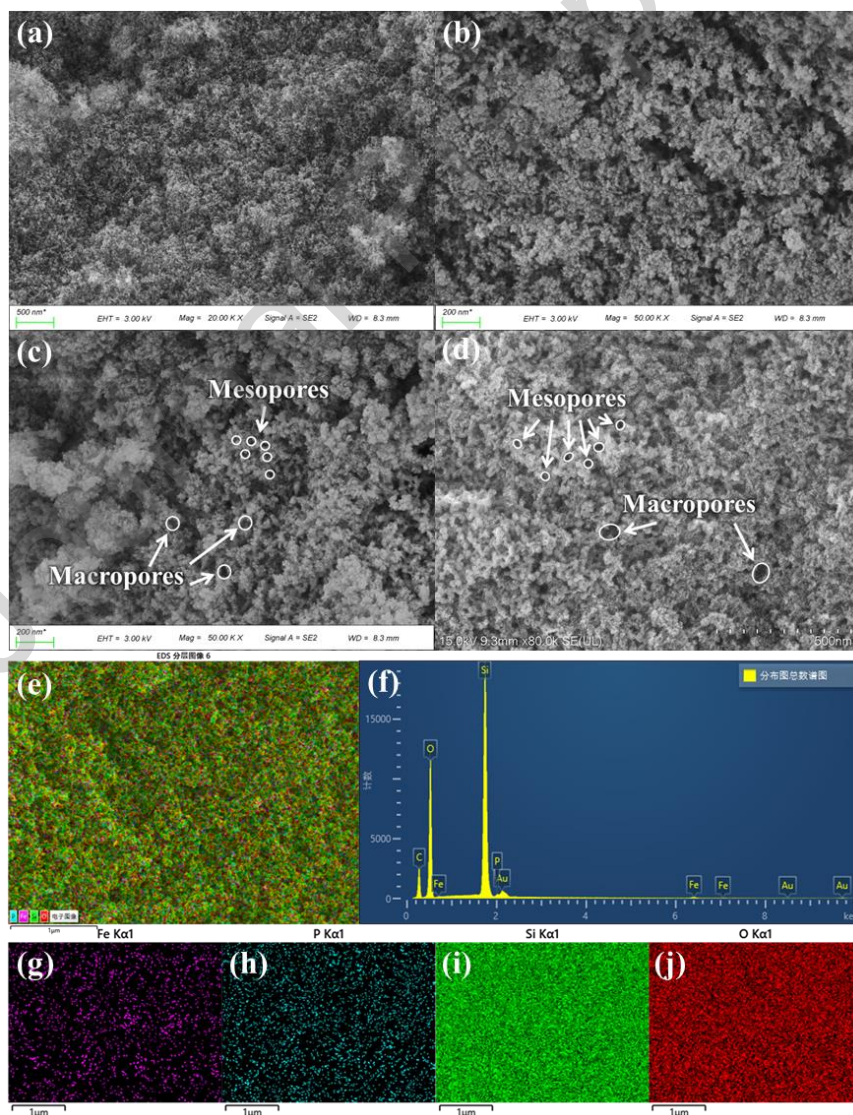

Fig. 4. (a~d) SEM images and (e~j) EDS mapping image of 4FPSA.

3.3. XRD analysis

Fig. 5(a~d) presents the XRD patterns of SA and FPSA with varying $FePO_x$ loadings. Within the SA's XRD pattern, a broad diffraction peak is evident at $2\theta = 22°$, denoting the existence of silica in its amorphous form. As the $FePO_x$ loading increases, the 2θ value corresponding to the silica characteristic peak shifts to a higher value[47]. With the increase of loading, some weak peaks appeared in the patterns. Notably, no distinct $FePO_x$ characteristic peaks manifest in the XRD patterns of FPSA across different loadings, which is in accordance with the previous literature studies. Combined with mapping image in 3.2, this absence might be attributed to the extensive dispersion of $FePO_x$ within the mesoporous channels or pore walls of the silica aerogel, rendering it elusive to XRD detection[48]. Fig. 5(e) shows the XRD pattern of 4FPSA heat-treated at 750°C, with weak characteristic peaks corresponding to $FePO_4$[49].
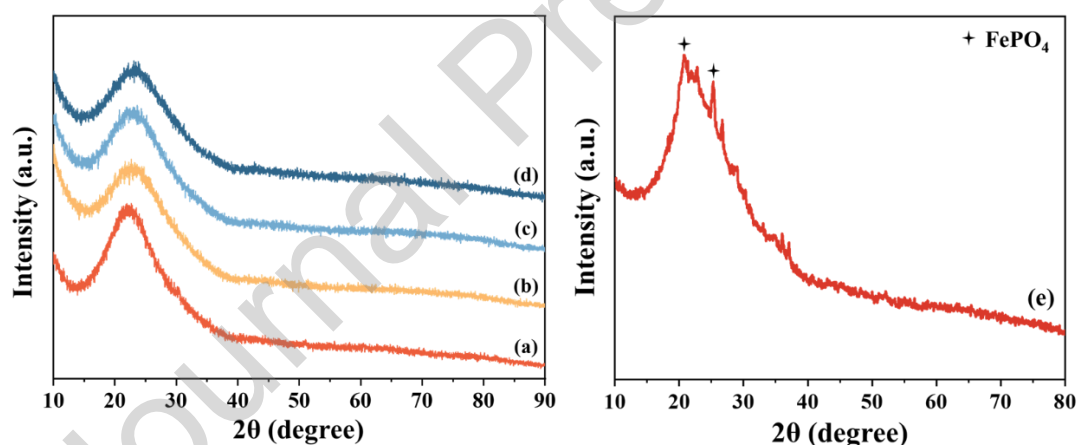

Fig. 5. XRD patterns of (a) SA, (b) 4FPSA, (c) 8FPSA, (d) 16FPSA, (e) 4FPSA-750°C.

3.4. FTIR analysis

Fig. 6 depicts the FTIR spectra of SA and FPSA across different loadings within the 400–2000 cm^{-1} range. The characteristic vibrational region around 470.63 cm^{-1} is ascribed to the Si-O symmetric bending vibration, while the absorption band close to 1097.64 cm^{-1} is attributed to the Si-O-Si asymmetric stretching vibration[11, 50]. Given the minimal content of Fe and P, no discernible absorption bands appear in the FTIR spectra. The displacement in the characteristic vibrational region in the FTIR spectra of

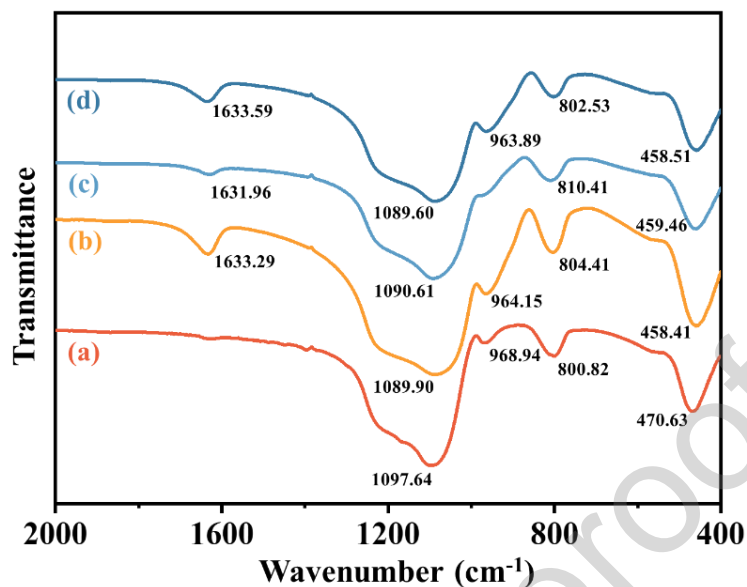various loadings corroborates the effective loading of the active component.

Fig. 6. FTIR spectra of (a) SA, (b) 4FPSA, (c) 8FPSA, (d) 16FPSA.

3.5. BET analysis

To investigate the specific surface area and pore structure of the sample, 4FPSA treated with varying temperatures was subjected to BET-BJH analysis. Fig. 7 presents the N_2-adsorption/desorption isotherms and the pore size distribution of 4FPSA across different heat treatment temperatures, with the accompanying data detailed in Table 1. All isotherms in Fig. 7(a) exhibit an H1-type hysteresis loop, classified as type IV isotherms, indicative of capillary condensation typical in mesoporous materials[51]. The saturation plateau in the adsorption isotherm signifies a uniform pore size distribution[52]. Combined with the BJH pore size distribution displayed in Fig. 7(b), the mean pore size of samples subjected to varying heat treatment temperatures lies between 12 and 16 nm. This reinforces the characterization of 4FPSA as a mesoporous material constituted of uniformly distributed spherical particles. There is a decline in the material's specific surface area as the heat treatment temperature escalates, a phenomenon ascribable to the high temperatures compromising the aerogel's pore structure. Upon a heat treatment at 550℃, the specific surface area for 4FPSA registers at 1175 m^2/g. An elevated specific surface area in the catalyst material can augment the dispersion of the active component, thereby enhancing the selectivity during catalytic
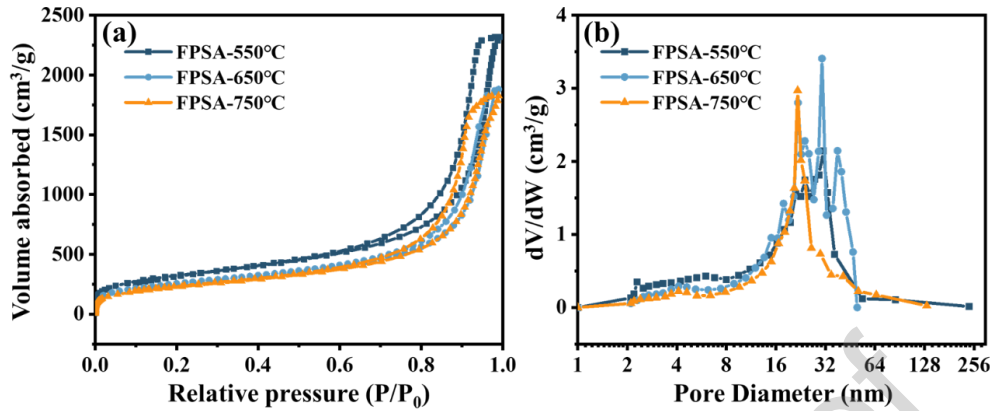
reactions.

Fig. 7. (a) N$_2$- adsorption/desorption isotherms, (b) pore size distribution curves of
4FPSA-550℃, 4FPSA-650℃, 4FPSA-750℃.

Table. 1 Pore structure of 4FPSA-550℃, 4FPSA-650℃, 4FPSA-750℃

Sample	BET surface area (m^2/g)	Average pore size (nm)
4FPSA-550℃	1175	12.5
4FPSA-650℃	925	15.2
4FPSA-750℃	830	13.3

3.6. Mechanical property analysis

To evaluate the mechanical properties of the materials, the compressive strain-stress
curves for block 4FPSA and SA were acquired, as depicted in Fig. 8. Silicon-oxide
based aerogels are widely recognized for their limited mechanical strength, often
fracturing immediately under applied pressure. Previous studies have documented a
compression modulus of approximately 0.13 MPa for pure silica aerogels produced
through traditional preparation techniques[53]. However, the compression modulus of
the pure silica aerogel SA, prepared using the methodology outlined in this study,
reached 1.33 MPa. Notably, the mechanical strength of 4FPSA surpassed that of SA,
registering a compression modulus of 7.56 MPa. This analysis suggests that materials
synthesized using the method detailed in this research exhibit enhanced mechanical
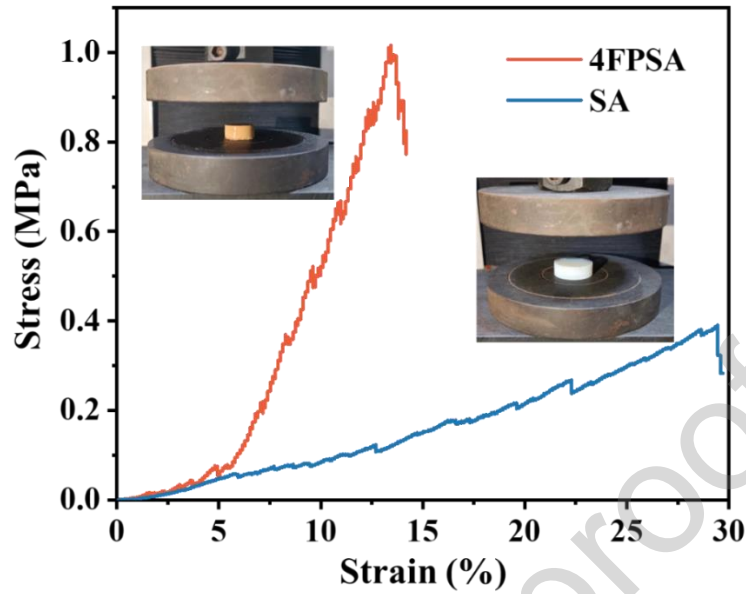
strength.

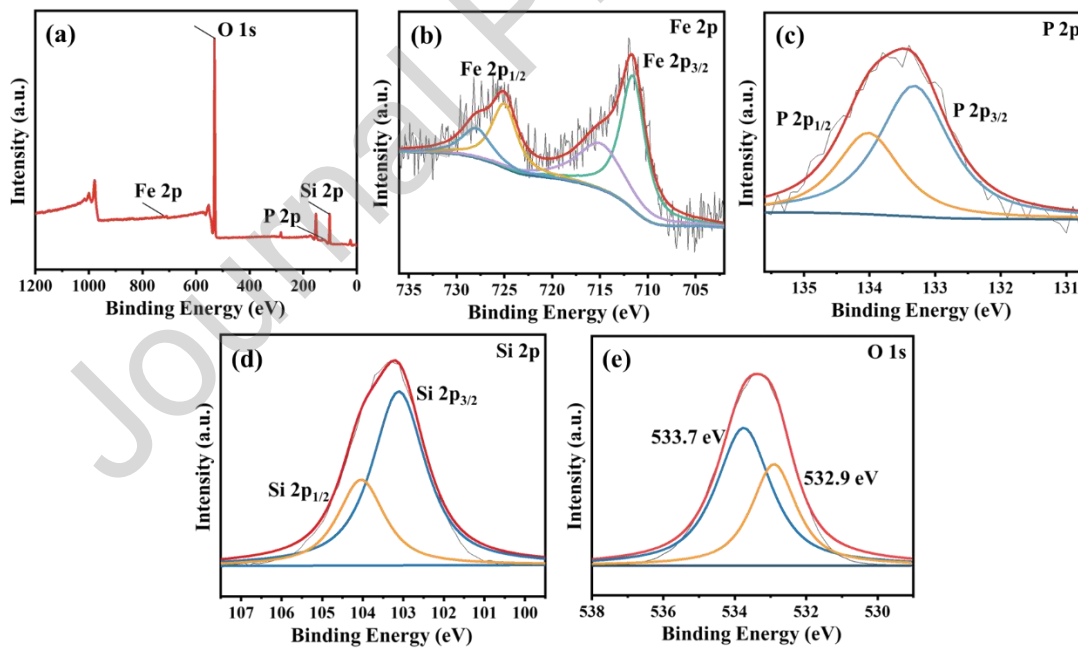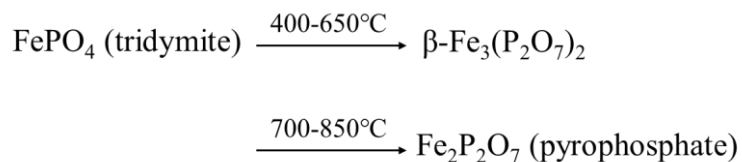Fig. 8. Compressive strain-stress curves of 4FPSA and SA

3.7. XPS analysis

Fig. 9. XPS spectra of (a) 4FPSA; High-resolution XPS spectra of (b) Fe 2p, (c) P 2p,

(d)Si 2P and (e) O1s of 4FPSA.

Elemental composition of the 4FPSA surface was elucidated through XPS analysis. Fig.

9 presents the full XPS spectrum of 4FPSA, complemented by the high-resolution XPS

spectra for Fe 2P, P 2P, Si 2P, and O 1s. In Fig. 9(a), the full XPS spectrum of 4FPSA displays characteristic peaks corresponding to each elemental component. The peak intensities of Fe 2P and P 2P are relatively low due to the low doping of Fe and P. Fig. 9(b) shows two characteristic peaks of the Fe 2P spectrum, corresponding to Fe $2p_{1/2}$ and Fe $2p_{3/2}$[54]. The Fe $2p_{3/2}$ peak, situated at 712.0 eV, predominantly signifies the vacancy generated from electron ionization in the 2p orbital of the iron atom, highlighting the Fe^{3+} oxidation state and corroborating the inclusion of Fe^{3+} in the sample[55, 56]. The Fe $2p_{1/2}$ peak exhibited enhanced sensitivity to alterations in the Fe chemical milieu than its Fe $2p_{3/2}$ counterpart. Fig. 9(c) depicts the P 2p peak positioned at 133.4 eV, wherein the peaks at 134.0 eV and 133.3 eV are ascribed to P $2p_{1/2}$ and P $2p_{3/2}$, respectively[54]. The O 1s spectrum, represented in Fig. 9(e), is characterized by two peaks: the peak at 532.9 eV pertains to surface hydroxyl oxygen, while the one at 533.7 eV is linked to lattice oxygen[57]. Surface hydroxyl oxygen, denoting surface adsorbed oxygen entities chemically bonded to surface atoms or molecules, exhibits significant chemical reactivity, playing a pivotal role in catalytic reactions and redox processes[58, 59].

3.8. H$_2$-TPR analysis

The catalytic activity of the material is inherently linked to its redox performance. The H$_2$-TPR technique was employed to assess the material's reduction performance across varying temperatures. As depicted in Fig. 10, H$_2$-TPR profiles for FPSA at diverse loadings reveal a reduction peak ranging between 200°C and 350°C, ascribed to the conversion of Fe^{3+} to Fe^{2+}[60]. To delve deeper into the phase transformations during reduction and oxidation processes, powder XRD and Mössbauer analyses were conducted on both reduced and oxidized $FePO_4$ specimens by the researchers. Peaks observed above 350°C are predominantly due to the transformation of $FePO_4$ to $Fe_2P_2O_7$[61, 62].

$$FePO_4 \text{ (tridymite)} \xrightarrow{400\text{-}650°C} \beta\text{-}Fe_3(P_2O_7)_2$$

$$\xrightarrow{700\text{-}850°C} Fe_2P_2O_7 \text{ (pyrophosphate)}$$

For the minimally loaded FPSA, the reduction peak manifested within a lower temperature spectrum. Notably, 4FPSA exhibited a pronounced reduction peak for the Fe^{3+} to Fe^{2+} transition, especially in the low temperature range. In the lower temperature range, the reduction signal decreased with increasing load. H_2-TPR results affirmed that the FPSA with lower loading exhibited a more potent reduction signal at a lower temperature. This observed pattern aligns with prior literature reports suggesting that highly dispersed, XRD-undetectable $FePO_4$ clusters potentially situated within the mesoporous channels of the catalyst support can undergo reduction at comparatively lower temperatures[48, 49]. A reduced loading augments the dispersion of the active component, enhancing the material's reduction efficacy at lower temperatures[63, 64].
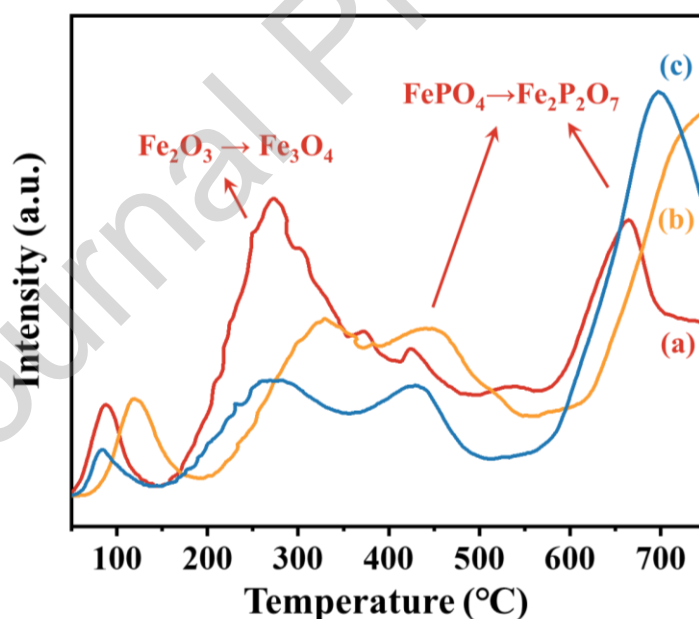

Fig. 10. H_2-TPR profiles of (a). 4FPSA, (b).8FPSA, (c).16FPSA.

3.9. Catalytic activity

Reduced loading augments the dispersion of the active components and thus enhances the material's reduction efficacy[63, 64], as confirmed in the testing of H_2-TPR. The catalytic performance of the catalysts with lower loading was assessed. The

performance of 4FPSA and 4FPSP as catalysts was evaluated in a fixed bed reactor. Table 2 delineates the catalytic reactions' outcomes, including CH_4 conversion along with the selectivity and yield of HCHO. Fig. 11 provides a comparative analysis.

Table. 2 Catalytic performance of 4FPSA and 4FPSP

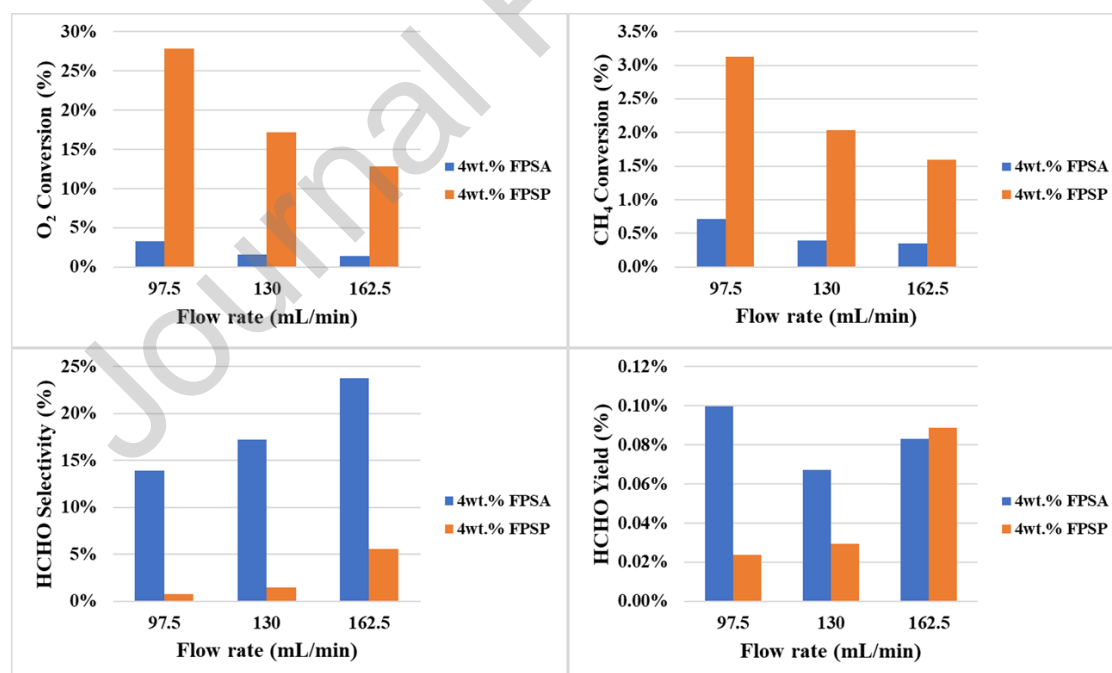| Catalyst	Flow rate (mL/min)	CH_4 Conversion	HCHO Selectivity	HCHO Yield
4FPSA	97.5	0.72%	13.92%	0.0997%
	130	0.39%	17.25%	0.0671%
	162.5	0.35%	23.75%	0.0832%
4FPSP	97.5	3.13%	0.76%	0.0237%
	130	2.03%	1.45%	0.0296%
	162.5	1.59%	5.58%	0.0888%

Fig. 11. Catalytic performance of 4FPSA and 4FPSP.

As the flow rate increased, the conversion of both O_2 and CH_4 diminished, while HCHO selectivity escalated. 4FPSP demonstrated a markedly superior CH_4 conversion compared to 4FPSA. This enhanced conversion can be attributed to the primary

distribution of active components on the SiO_2 support surface in the 4FPSP catalyst. A more extensive contact area between the active component and the reaction gas culminates in this elevated CH_4 conversion. Conversely, 4FPSA manifests a more pronounced HCHO selectivity, which can be linked to the mass transfer limitations appeared with the larger particles present in 4FPSP. Established knowledge suggests that, within catalytic systems undergoing series reactions, mass transfer limitations cause a decline in selectivity for intermediary compounds[65-67]. SEM and XRD analyses for 4FPSA indicate that the active components Fe and P in the catalyst are thoroughly dispersed within porous SiO_2, predominantly residing in the mesoporous channels or pore walls of the silica aerogel support. Such a distribution result in diminished CH_4 conversion but accentuated HCHO selectivity. At flow rates of 97.5 mL/min, 130 mL/min, and 162.5 mL/min, HCHO selectivity for 4FPSA exceeded that of 4FPSP by factors of 18.3, 11.9, and 4.3 respectively. Furthermore, at flow rates of 97.5 mL/min and 130 mL/min, HCHO yield for 4FPSA surpassed that of 4FPSP by 4.2 and 2.3 times, respectively.

4. Conclusion

In summary, FPSA was synthesized utilizing a combination of heating reflux, sol-gel technique, and supercritical ethanol drying process. These aerogel materials boast an exceptionally high specific surface area and ensure optimal dispersion of Fe and P on porous SiO_2. The size of the spherical aerogel are controllable. The composite's specific surface area reached an impressive 1175 m^2/g, and the compression modulus of 7.56 MPa surpassed that of the aerogel produced through conventional methods. These performances are outperform the majority of existing literature studies. Catalyst materials with lower loading displayed a pronounced reduction signal at a lower temperatures. Enhanced dispersion of the active components contributed to the elevation of HCHO selectivity in catalyst materials. Under conditions of a reaction temperature of 650℃ and a flow rate of 97.5 mL/min, the HCHO selectivity and yield for 4FPSA were 18.3 and 4.2 times greater than those of 4FPSP, respectively. This research offers a valuable benchmark for the synthesis of silica-based aerogels with

ultra-high specific surface areas and introduces a novel approach for the direct catalytic oxidation of methane using silica-based catalyst materials.

Acknowledgments

References

[1] A. S. Dorcheh, M. Abbasi, Silica aerogel; synthesis, properties and characterization, J. Mater. Process. Technol., 199 (2008) 10-26.

[2] J. L. Gurav, I. K. Jung, H. H. Park, E. S. Kang, D. Y. Nadargi, Silica Aerogel: Synthesis and Applications, J. Nanomater., 2010 (2010) 23.

[3] S. Cui, W. Cheng, X. Shen, M. Fan, A. T. Russell, Z. Wu, X. Yi, Mesoporous amine-modified SiO_2 aerogel: a potential CO_2 sorbent, Energy Environ. Sci., 4 (2011) 2070-2074.

[4] V. G. Parale, T. Kim, K. Y. Lee, V. D. Phadtare, R. P. Dhavale, H. N. R. Jung, H. H. Park, Hydrophobic TiO_2-SiO_2 composite aerogels synthesized via in situ epoxyring opening polymerization and sol-gel process for enhanced degradation activity, Ceram. Int., 46 (2020) 4939-4946.

[5] H. Liu, X. Chen, Y. Zheng, D. Zhang, Y. Zhao, C. Wang, C. Pan, C. Liu, C. Shen, Lightweight, superelastic, and hydrophobic polyimide nanofiber/MXene composite aerogel for wearable piezoresistive sensor and oil/water separation applications, Adv. Funct. Mater., 31 (2021) 2008006.

[6] H. Sai, L. Xing, J. Xiang, L. Cui, F. Li, Flexible aerogels based on an interpenetrating network of bacterial cellulose and silica by a non-supercritical drying process, J. Mater. Chem. A, 1 (2013) 7963-7970.

[7] J. Shi, L. Lu, W. Guo, J. Zhang, Y. Cao, Heat insulation performance, mechanics and hydrophobic modification of cellulose-SiO$_2$ composite aerogels, Carbohydr. Polym., 98 (2013) 282-289.

[8] W. Yan, Y. Liu, G. Shao, K. Zhu, S. Cui, W. Wang, X. Shen, Chemical surface adsorption and trace detection of alcohol gas in graphene oxide-based acid-etched SnO$_2$ aerogels, ACS Appl. Mater. Inter., 13 (2021) 20467-20478.

[9] S. Liu, T. Jiang, M. Fan, G. Tan, S. Cui, X. Shen, Nanostructure rod-like TiO$_2$-reduced graphene oxide composite aerogels for highly-efficient visible-light photocatalytic CO$_2$ reduction, J. Alloys Compd., 861 (2021) 158598.

[10] S. Liu, K. Zhu, S. Cui, X. Shen, G. Tan, A novel building material with low thermal conductivity: Rapid synthesis of foam concrete reinforced silica aerogel and energy performance simulation, Energy Build., 177 (2018) 385-393.

[11] Z. Zhao, Y. Cui, Y. Kong, J. Ren, X. Jiang, W. Yan, M. Li, J. Tang, X. Liu, X. Shen, Thermal and mechanical performances of the superflexible, hydrophobic, silica-based aerogel for thermal insulation at ultralow temperature, ACS Appl. Mater. Inter., 13 (2021) 21286-21298.

[12] J. He, X. Li, D. Su, H. Ji, X. Wang, Ultra-low thermal conductivity and high strength of aerogels/fibrous ceramic composites, J. Eur. Ceram. Soc., 36 (2016) 1487-1493.

[13] W. Mei, Preparation and properties of SiO$_2$ aerogel and fabric composite based on polyurethane, Integr. Ferroelectr., 189 (2018) 36-43.

[14] F. Peng, Y. Feng, J. Cai, H. Feng, J. Li, L. Jun, Thermally insulating, fiber-reinforced alumina-silica aerogel composites with ultra-low shrinkage up to 1500 degrees C, Chem. Eng. J., 411 (2021) 128402.

[15] L. Tong, J. Lou, R. R. Gattass, S. He, X. Chen, Liu, E. Mazur, Assembly of silica nanowires on silica aerogels for microphotonic devices, Nano Lett., 5 (2005) 259–262.

[16] L. Xiao, M. Grogan, S. Leon-Saval, R. Williams, R. England, W. Wadsworth, T. Birks, Tapered fibers embedded in silica aerogel, Opt. Lett., 34 (2009) 2724-2726.

[17] F. Yang, J. Zhu, X. Zou, X. Pang, R. Yang, S. Chen, Y. Fang, T. Shao, X. Luo, L. Zhang, Three-dimensional TiO$_2$/SiO$_2$ composite aerogel films via atomic layer deposition with enhanced H$_2$S gas sensing performance, Ceram. Int., 44 (2018) 1078-1085.

[18] W. Yan, Y. Liu, G. Shao, K. Zhu, S. Cui, W. Wang, X. Shen, Chemical Surface Adsorption and Trace Detection of Alcohol Gas in Graphene Oxide-Based Acid-Etched SnO$_2$ Aerogels, ACS Appl. Mater. Inter., 13 (2021) 20467-20478.

[19] W. Yan, K. Zhu, Y. Cui, Y. Li, X. Shen, NO$_2$ detection and redox capacitance reaction of Ag doped SnO$_2$/rGO aerogel at room temperature, J. Alloys Compd., 886 (2021) 161287.

[20] K. Zhu, W. Yan, S. Liu, X. Wu, S. Cui, X. Shen, One-step hydrothermal synthesis of MnO$_x$-CeO$_2$/reduced graphene oxide composite aerogels for low temperature selective catalytic reduction of NO$_x$, Appl. Surf. Sci., 508 (2020) 145024.

[21] F. Peng, Y. Jiang, J. Feng, L. Li, J. Feng, A facile method to fabricate monolithic alumina–silica aerogels with high surface areas and good mechanical properties, J. Eur. Ceram. Soc., 40 (2020) 2480-2488.

[22] X. Du, C. Wang, T. Li, M. Chen, Studies on the performances of silica aerogel electrodes for the application of supercapacitor, Ionics, 15 (2009) 561-565.

[23] D. Kim, S. Jung, H. Jung, A super-thermostable, flexible supercapacitor for ultralight and high performance devices, J. Mater. Chem. A, 8 (2020) 532-542.

[24] J. Ren, J. Zhou, Y. Kong, X. Jiang, X. Shen, Development of Regular Hydrophobic Silica Aerogel Microspheres for Efficient Oil Adsorption, Langmuir, 39 (2022) 478–486.

[25] S. Zhao, G. Siqueira, S. Drdova, D. Norris, C. Ubert, A. Bonnin, S. Galmarini, M. Ganobjak, Z. Pan, S. Brunner, G. Nyström, J. Wang, M. M. Koebel, W. J. Malfait, Additive manufacturing of silica aerogels, Nature, 584 (2020) 387-392.

[26] L. Ding, B. Yao, F. Li, S. Shi, N. Huang, H. Yin, Q. Guan, Y. Dong, Ionic liquid-decorated COF and its covalent composite aerogel for selective CO_2 adsorption and catalytic conversion, J. Mater. Chem. A, 7 (2019) 4689-4698.

[27] C. Kim, K. M. Cho, K. Park, J. Y. Kim, G. T. Yun, F. M. Toma, I. Gereige, H. T. Jung, Cu/Cu_2O interconnected porous aerogel catalyst for highly productive electrosynthesis of ethanol from CO_2, Adv. Funct. Mater., 31 (2021) 2102142.

[28] T. Kim, S. Roy, S. Moon, S. Yoo, H. Choi, V. Parale, Y. Kim, J. Lee, S. Jun, K. Kang, Highly Dispersed Pt Clusters on F-Doped Tin (IV) Oxide Aerogel Matrix: An Ultra-Robust Hybrid Catalyst for Enhanced Hydrogen Evolution, ACS Nano, 16 (2022) 1625-1638.

[29] J. Amonette, J. Matyáš, Functionalized silica aerogels for gas-phase purification, sensing, and catalysis: A review, Microporous Mesoporous Mater., 250 (2017) 100-119.

[30] J. Arfaoui, A. Ghorbel, C. Petitto, G. Delahay, Promotional effect of ceria on the catalytic behaviour of new V_2O_5–WO_3–TiO_2 aerogel solids for the $DeNO_x$ process, J. Solid State Chem., 300 (2021) 122261.

[31] S. Daneshmand-Jahromi, M. Sedghkerdar, N. Mahinpey, Synthesis, characterization, and kinetic study of nanostructured copper-based oxygen carrier supported on silica and zirconia aerogels in the cyclic chemical looping combustion process, Chem. Eng. J., 448 (2022) 137756.

[32] G. Shao, X. Shen, X. Huang, Multilevel Structural Design and Heterointerface Engineering of a Host–Guest Binary Aerogel toward Multifunctional Broadband Microwave Absorption, ACS Mater. Lett., 4 (2022) 1787-1797.

[33] G. Shao, C. Ding, G. Yu, R. Xu, X. Huang, Bridged polysilsesquioxane-derived SiOCN ceramic aerogels for microwave absorption, J. Am. Ceram. Soc., 106 (2023) 2407-2419.

[34] G. Shao, D. Hanaor, X. Shen, A. Gurlo, Freeze casting: from low-dimensional building blocks to aligned porous structures-a review of novel materials, methods, and applications, Adv. Mater., 32 (2020) 1907176.

[35] Y. Sun, J. Huang, D. Shi, S. Zhang, Z. Fu, T. Fan, L. Dong, X. Zheng, L. Zhou, X. He, X. Yang, Tension and compression moduli characterization of a bimodular ceramic-fiber reinforced SiO_2 aerogel composite, Mater. Test., 62 (2020) 1003-1009.

[36] X. Zhang, X. Cheng, Y. Si, Elastic and highly fatigue resistant ZrO_2-SiO_2 nanofibrous aerogel with low energy dissipation for thermal insulation, Chem. Eng. J., 433 (2022) 133628.

[37] H. Yu, Y. Jiang, Y. Lu, X. Li, H. Zhao, Y. Ji, M. Wang, Quartz fiber reinforced Al_2O_3-SiO_2 aerogel composite with highly thermal stability by ambient pressure drying, J. Non-Cryst. Solids, 505 (2019) 79-86.

[38] Y. Lei, Z. Hu, B. Cao, X. Chen, H. Song, Enhancements of thermal insulation and mechanical property of silica aerogel monoliths by mixing graphene oxide, Mater. Chem. Phys., 187 (2017) 183-190.

[39] H. Maleki, L. Duraes, A. Portugal, Development of mechanically strong ambient pressure dried silica aerogels with optimized properties, J. Phys. Chem. C, 119 (2015) 7689-7703.

[40] J. Feng, Q. Gao, C. Zhang, Y. Jiang, Effect of SiO_2 sol proportion on the mechanical properties of aerogel insulation composites, Fuhe Cailiao Xuebao/Acta Materiae Compositae Sinica, 27 (2010) 179-183.

[41] J. Zhu, J. Hu, C. Jiang, S. Liu, Y. Li, Ultralight, hydrophobic, monolithic konjac glucomannan-silica composite aerogel with thermal insulation and mechanical properties, Carbohydr. Polym., 207 (2018) 246-255.

[42] X. Hou, R. Zhang, D. Fang, An ultralight silica-modified ZrO_2-SiO_2 aerogel composite with ultra-low thermal conductivity and enhanced mechanical strength, Scripta Mater., 143 (2018) 113-116.

[43] S. Shafi, R. Navik, X. Ding, Y. Zhao, Improved heat insulation and mechanical properties of silica aerogel/glass fiber composite by impregnating silica gel, J. Non-Crys. Solids, 503 (2019) 78-83.

[44] Z. Li, X. Cheng, S. He, X. Shi, L. Gong, H. Zhang, Aramid fibers reinforced silica aerogel composites with low thermal conductivity and improved mechanical performance, Compos. Part A-Appl. S., 84 (2016) 316-325.

[45] Q. Zhang, L. Yang, D. An, W. Ye, Catalytic behavior and kinetic features of FeO_x/SBA-15 catalyst for selective oxidation of methane by oxygen, Appl. Catal. A-Gen., 356 (2009) 103-111.

[46] J. He, Y. Li, D. An, Q. Zhang, Y. Wang, Selective oxidation of methane to formaldehyde by oxygen over silica-supported iron catalysts, J. Nat. Gas Chem., 18(2009) 288–294.

[47] W. Puthai, M. Kanezashi, H. Nagasawa, T. Tsuru, SiO_2-ZrO_2 nanofiltration membranes of different Si/Zr molar ratios: Stability in hot water and acid/alkaline solutions, J. Membr. Sci., 524 (2017) 700-711.

[48] X. Wang, Y. Wang, Q. Tang, Q. Guo, Q. Zhang, H. Wan, MCM-41-supported iron phosphate catalyst for partial oxidation of methane to oxygenates with oxygen and nitrous oxide, J. Catal., 217 (2003) 457-467.

[49] Y. Wang, X. Wang, Z. Su, Q. Guo, Q. Tang, Q. Zhang, H. Wan, SBA-15-supported iron phosphate catalyst for partial oxidation of methane to formaldehyde, Catal. Today, 93 (2004) 155-161.

[50] R. Al-Oweini, H. El-Rassy, Synthesis and characterization by FTIR spectroscopy of silica aerogels prepared using several Si (OR)$_4$ and R''Si (OR')$_3$ precursors, J. Mol. Struct., 919 (2009) 140-145.

[51] T. Horikawa, D. Do, D. Nicholson, Capillary condensation of adsorbates in porous materials, Adv. Colloid Interface Sci., 169 (2011) 40-58.

[52] P. Selvam, S. K. Bhatia, C. G. Sonwane, Recent advances in processing and characterization of periodic mesoporous MCM-41 silicate molecular sieves, Ind. Eng. Chem. Res., 40 (2001) 3237-3261.

[53] Y. Lei, Z. Hu, B. Cao, X. Chen, H. Song, Enhancements of thermal insulation and mechanical property of silica aerogel monoliths by mixing graphene oxide, Mater. Chem. Phys., 187 (2017) 183-190.

[54] Y. Zhang, C. Huang, H. Min, H. Shu, P. Gao, Q. Liang, X. Yang, L. Liu, X. Wang, Bowl-like double carbon layer architecture of hollow carbon@$FePO_4$@reduced graphene oxide composite as high-performance cathodes for sodium and lithium ion batteries, J. Alloys Compd., 795 (2019) 34-44.

[55] P. Mills, J. Sullivan, A study of the core level electrons in iron and its three oxides by means of X-ray photoelectron spectroscopy, J. Phys. D: Appl. Phys., 16 (1983) 723.

[56] M. Descostes, F. Mercier, N. Thromat, C. Beaucaire, M. Gautier-Soyer, Use of XPS in the determination of chemical environment and oxidation state of iron and sulfur samples: constitution of a data basis in binding energies for Fe and S reference compounds and applications to the evidence of surface species of an oxidized pyrite in a carbonate medium, Appl. Surf. Sci., 165 (2000) 288-302.

[57] Y. Liu, Z. Li, Y. You, X. Zheng, J. Wen, Synthesis of different structured $FePO_4$ for the enhanced conversion of methyl cellulose to 5-hydroxymethylfurfural, RSC Adv., 7 (2017) 51281-51289.

[58] X. Guo, W. Ding, H. Chen, Q. Yan, Preparation and Characterization of Nanosized Fe-P-O Catalyst, Journal of Fuel Chemistry and Technology, 28 (2000) 385-387.

[59] C. Chen, Q. Chen, Y. Li, J. Yang, B. Huang, X. Liu, X. Xing, S. Xiao, S. Chen, R. Wang, Microspherical $LiFePO_{3.98}F_{0.02}$/3DG/C as an advanced cathode material for high-energy lithium-ion battery with a superior rate capability and long-term cyclability, Ionics, 27 (2021) 1-11.

[60] R. Lin, Y. Ding, L. Gong, W. Dong, W. Chen, Y. Lu, Studies on oxy-bromination of methane and coke deposition over $FePO_4$/SiO_2 catalysts, Catal. Today, 164 (2011) 34-39.

[61] V. D. B. C. Dasireddy, D. Hanzel, K. Bharuth-Ram, B. Likozar, The effect of oxidant species on direct, non-syngas conversion of methane to methanol over an $FePO_4$ catalyst material, RSC Adv., 9 (2019) 30989-31003.

[62] F. B. Khan, K. Bharuth-Ram, H. B. Friedrich. Phase transformations of the $FePO_4$ catalyst in the oxidative dehydrogenation to form an alkyl methacrylate, Hyperfine Interact., 197 (2010) 317-323.

[63] T. Kobayashi, K. Nakagawa, K. Tabata, M. Haruta, Partial oxidation of methane over silica catalysts promoted by 3d transition metal ions, J. Chem. Soc., Chem. Commun., 13 (1994) 1609-1610.

[64] C. Fajardo, D. Niznansky, Y. N'Guyen, C. Courson, A. C. Roger, Methane selective oxidation to formaldehyde with Fe-catalysts supported on silica or incorporated into the support, Catal. Commun., 9 (2008) 864-869.

[65] J. A. Baeza，F. Garcia-Missana，A. S. Oliveira，L. Calvo，M. A. Gilarranz, Influence of H_2 availability in the catalytic reduction of nitrates in fixed bed reactors, Chem. Eng. Sci., 246 (2021) 116887.

[66] D. T. González，A. Marí，J. A. Baeza，L. Calvo，M. A. Gilarranz, Enhancement of activity and selectivity to nitrogen in catalytic nitrate reduction by use of conductive carbon catalytic supports and control of hydrogen mass transfer regime, J. Environ. Chem. Eng., 9 (2021) 106419.

[67] C. Zhang，S. Yan，J. Lin，Q. Hu，J. Zhong，B. Zhang，Z. Cheng, Electrochemical Reduction of CO_2 to CO on Hydrophobic Zn Foam Rod in a Microchannel Electrochemical Reactor, Processes, 9 (2021) 1592.

Graphical abstract
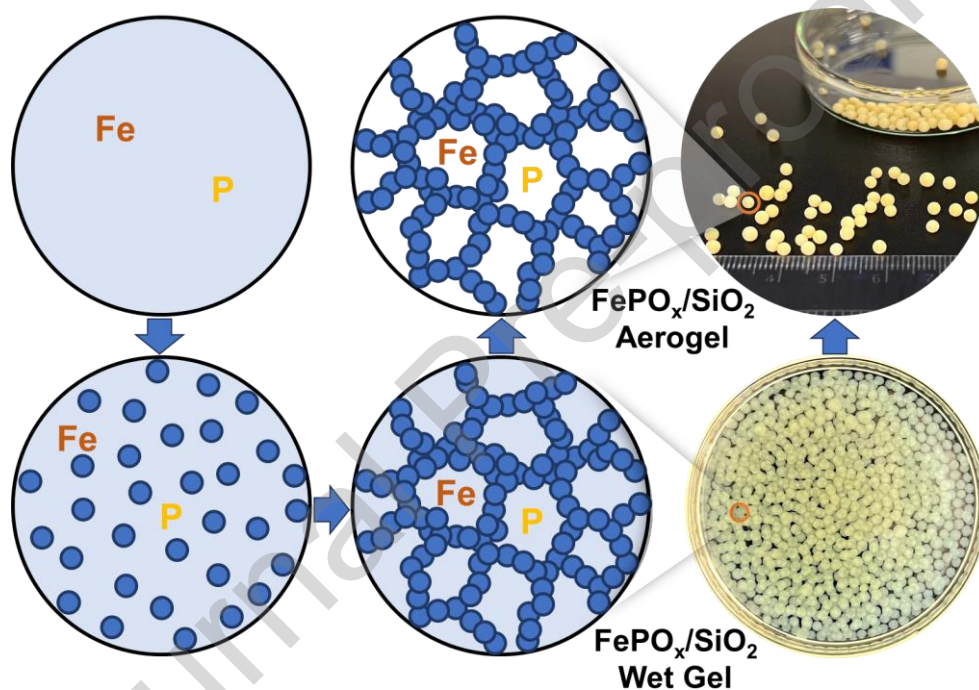
Credit Author Statement

We declare that we do not have any commercial or associative interest that represents a conflict of interest in connection with the work submitted. To the best of our knowledge and belief, this work is original and this manuscript has not been published in whole or in part nor is it being considered for publication elsewhere. In addition, all authors have read the manuscript and approved to submit to your journal.

Highlights

- Spherical $FePO_x/SiO_2$ aerogel was synthesized by heating reflux and sol-gel method.

- The active components were highly dispersed on a porous SiO_2 aerogel support.

- 4FPSA has an ultra-high specific surface area (1174.71 m^2/g) and a high compression modulus (7.56 MPa).

- The 4FPSA has an 18. 3 times higher HCHO selectivity than 4FPSP.